Monthly Notices
of the
ROYAL ASTRONOMICAL SOCIETY

MNRAS **486,** 2366–2378 (2019)
Advance Access publication 2019 April 18

doi:10.1093/mnras/stz945

The molecular gas properties in the gravitationally lensed merger HATLAS J142935.3–002836

Hugo Messias [1,2]★ Neil Nagar,[3] Zhi-Yu Zhang,[4] Iván Oteo,[4,5] Simon Dye [6] Eduardo Ibar,[7] Nicholas Timmons,[8] Paul van der Werf,[9] Dominik Riechers [10] Stephen Eales,[11] Rob Ivison,[4,5] Jacob Maresca [6] Michał J. Michałowski [12] and Chentao Yang [2]

[1]*Joint ALMA Observatory, Alonso de Córdova 3107, Vitacura 763-0355, Santiago, Chile*
[2]*European Southern Observatory, Alonso de Córdova 3107, Vitacura, Casilla 19001, Santiago de Chile, Chile*
[3]*Astronomy Department, Universidad de Concepción, Barrio Universitario S/N, Concepción, Chile*
[4]*European Southern Observatory, Karl-Schwarzschild-Str 2, D-85748 Garching, Germany*
[5]*Institute for Astronomy, University of Edinburgh, Royal Observatory, Blackford Hill, Edinburgh EH9 3HJ, UK*
[6]*School of Physics and Astronomy, University of Nottingham, University Park, Nottingham NG7 2RD, UK*
[7]*Instituto de Física y Astronomía, Universidad de Valparaíso, Avda. Gran Bretaña 1111, Valparaíso, Chile*
[8]*Department of Physics and Astronomy, University of California, Irvine, CA 92697, USA*
[9]*Leiden Observatory, Leiden University, PO Box 9513, NL-2300 RA Leiden, the Netherlands*
[10]*Cornell University, Space Sciences Building, Ithaca, NY 14853, USA*
[11]*School of Physics and Astronomy, Cardiff University, The Parade, Cardiff CF24 3AA, UK*
[12]*Astronomical Observatory Institute, Faculty of Physics, Adam Mickiewicz University, ul. Słoneczna 36, PL-60-286 Poznań, Poland*

Accepted 2019 March 27. Received 2019 March 26; in original form 2019 January 25

ABSTRACT

Follow-up observations of (sub-)mm-selected gravitationally lensed systems have allowed a more detailed study of the dust-enshrouded phase of star formation up to very early cosmic times. Here, the case of the gravitationally lensed merger in HATLAS J142935.3–002836 (also known as H1429−0028; $z_{\rm lens} = 0.218$, $z_{\rm bkg} = 1.027$) is revisited following recent developments in the literature and new Atacama Pathfinder EXperiment (APEX) observations targeting two carbon monoxide (CO) rotational transitions $J_{\rm up} = 3$ and 6. We show that the line profiles comprise three distinct velocity components, where the fainter high velocity one is less magnified and more compact. The modelling of the observed spectral line energy distribution of CO $J_{\rm up} = 2$–6 and [C I] $^3P_1-^3P_0$ assumes a large velocity gradient scenario, where the analysis is based on four statistical approaches. Since the detected gas and dust emission comes exclusively from only one of the two merging components (the one oriented north–south, NS), we are only able to determine upper limits for the companion. The molecular gas in the NS component in H1429−0028 is found to have a temperature of ∼70 K, a volume density of $\log(n[{\rm cm}^{-3}]) \sim 3.7$, to be expanding at ∼10 km s^{-1} pc^{-1}, and amounts to $M_{\rm H_2} = 4^{+3}_{-2} \times 10^9\,{\rm M}_\odot$. The CO to H_2 conversion factor is estimated to be $\alpha_{\rm CO} = 0.4^{+0.3}_{-0.2}\ {\rm M}_\odot/({\rm K\ km\ s^{-1}\ pc^2})$. The NS galaxy is expected to have a factor of $\gtrsim$10× more gas than its companion ($M_{\rm H_2} \lesssim 3 \times 10^8\,{\rm M}_\odot$). Nevertheless, the total amount of molecular gas in the system comprises only up to 15 per cent (1σ upper limit) of the total (dynamical) mass.

Key words: gravitational lensing: strong – ISM: abundances – galaxies: interactions – submillimetre: galaxies – submillimetre: ISM.

1 INTRODUCTION

Understanding the life cycle of galaxies necessitates an observational multiwavelength approach, not only due to the many evolution tracks a galaxy may follow (e.g. finishing as an early-type galaxy,

★ E-mail: hugo.messias@alma.cl

or as an 'untouched' disc galaxy as NGC 1277; Trujillo et al. 2014), but also the many physical mechanisms at play (e.g. star formation and its quenching, heavy elements production), and the advantages and disadvantages specific to different methods of analysis.

Specifically, the brightest of the dusty star-forming galaxies (DSFGs; see Casey, Narayanan & Cooray 2014, for a review), also referred to as submillimetre galaxies (SMGs; Smail, Ivison & Blain 1997; Hughes et al. 1998), provide a strong case for the early active evolution stages of the most massive galaxies seen in the local Universe (e.g. Simpson et al. 2014; Toft et al. 2014). Despite not being representative of the whole galaxy population, SMGs may enable us to unveil the dusty origins of the local Universe's massive monsters, as seen in a Universe with less than 25 per cent its current age ($z \gtrsim 2$). They are highly star forming and already massive galaxies, quickly exhausting their large gas reservoirs, and with a source density comparable to massive galaxies in the local Universe (Casey et al. 2014). Whether or not the SMG phase is responsible for the build-up of the bulk of the stellar populations in massive galaxies today is still a matter of active discussion, but what is clear is that this short-lived phase can indeed induce a significant galaxy growth in relatively small cosmological time intervals (∼100 Myr).

A useful characteristic of DSFGs is that, among the brightest of their kind, there are easily selected strongly lensed systems (Negrello et al. 2010; Vieira et al. 2010; Wardlow et al. 2013) that can be exploited to probe this intriguing galaxy population down to fainter fluxes and higher resolution. These chance alignments are nevertheless rare (less than one per deg^2; Negrello et al. 2010) and require wide field surveys. These have been possible in recent years with facilities such as the *Herschel Space Observatory* (*Herschel*), South Pole Telescope (SPT), or *Planck*, which enabled $>$ 100 deg^2 surveys at far-infrared (FIR) to millimetre (mm) wavelengths. The *Herschel* Astrophysical Terahertz Large Area Survey (HATLAS; Eales et al. 2010) has covered different patches of the 100–500 μm sky amounting to 570 deg^2. The *Herschel* Stripe 82 Survey (HerS; Viero et al. 2014) and the HerMES Large Mode Survey (HeLMS; Oliver et al. 2012) covered, respectively, 280 and 95 deg^2 of the sky at 250–500 μm. The SPT covered 2500 deg^2 of the southern sky at 1–3 mm (Williamson et al. 2011). Finally, the *Planck* mission covered the whole sky at 0.35–10 mm (Planck Collaboration I 2016).

There are now numerous cases of gravitationally lensed galaxies for exploration of the finer details of galaxy evolution at earlier times. This is done by intensive follow-up campaigns of these systems, for instance, via high-resolution multiwavelength imaging enabling rest-frame optical to FIR reconstruction of the background source plane (e.g. Negrello et al. 2010; Calanog et al. 2014; Messias et al. 2014; Timmons et al. 2016), or optical to mm spectroscopy to constrain the distances to lens and lensed galaxies (e.g. Scott et al. 2011; Lupu et al. 2012; Vieira et al. 2013; Strandet et al. 2016; Negrello et al. 2017) and the gas conditions and content of the star-bursting background systems (e.g. Riechers et al. 2011; Harris et al. 2012; Timmons et al. 2015; Bothwell et al. 2017; Oteo et al. 2017a; Strandet et al. 2017; Yang et al. 2017; Cañameras et al. 2018; Motta et al. 2018).

1.1 The HATLAS J142935.3–002836 case

This paper reports the latest advances in comprehending the gravitationally lensed system in HATLAS J142935.3–002836 (also known as H1429−0028; Messias et al. 2014, hereafter M14). M14 reported the initial findings on H1429−0028 that appeared as the brightest of an early set of candidates for gravitationally lensed galaxies in HATLAS (an observed FIR flux at 160 μm of $S_{160\,\mu m} \sim 1.2$ Jy). It was found that H1429−0028 comprises an edge-on disc galaxy at $z = 0.218$ acting as lens, surrounded by an almost complete Einstein ring with a 3–4 knot morphology. Subarcsec imaging at near-IR to radio wavelengths enabled reconstruction of the background source to reveal a merging system magnified by an overall factor of ∼10 and comprising two distinct galaxies at $z = 1.027$ (M14). One galaxy has an east–west orientation dominating the rest-frame optical spectral range (henceforth known as the EW galaxy/component). The other, appearing north–south oriented and with a compact intrinsic half-light radius $r_{1/2} = 0.9 \pm 0.3$ kpc, dominates the gaseous and dusty content of the system, being the main contributor to the long-wavelength spectral regime flux (henceforth known as the NS galaxy/component). In Dye et al. (2018), the magnification factor of the dust component in NS was revised to be ∼23, further highlighting the need for proper magnification lensing analysis incorporating complex morphologies. Fig. 1 shows a toy model to help understand the background system. Specifically the inset shows the velocity map of the NS galaxy, where it is clear that its southern region is more blueshifted than the northern one where a peak in velocity dispersion is seen (M14). A more detailed discussion can be found in M14 (specifically, figs 1 and 8 therein).

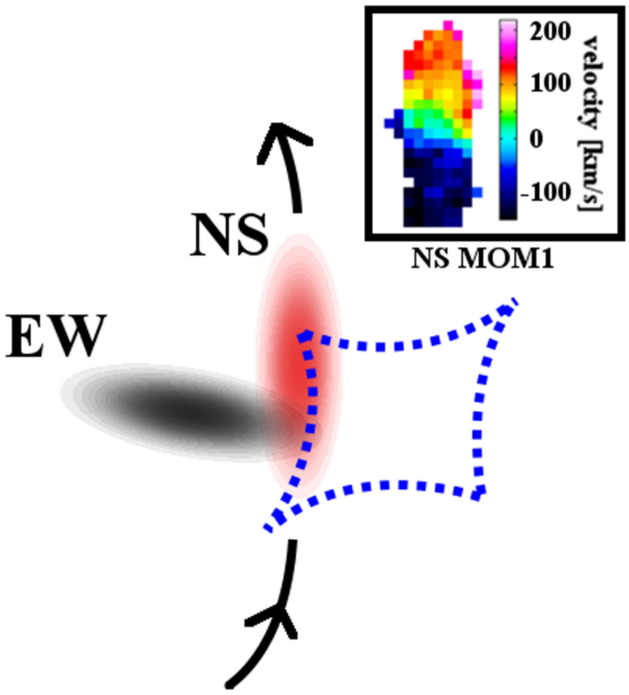

Figure 1. This toy model shows a simplified view of the background merger in H1429−0028. The east–west oriented galaxy (EW) dominates the rest-frame optical spectral range, while the north–south oriented one (NS) dominates the long-wavelength spectral regime. The caustic is overlaid as a dashed blue line. The currently inferred impact direction is indicated with the black arrows (see Section 4.1). The inset shows the velocity map (moment-1) of the NS galaxy (M14), where the colour bar extends from −150 to 150 km s^{-1}.

In M14, the information available at the time only allowed for the determination of the expected range of molecular gas content. As a result, Atacama Pathfinder EXperiment (APEX) observations were conducted to observe extra carbon monoxide (CO) transitions, thus improving its spectral line energy distribution (SLED), together with the already observed [C I] $^3P_1 - ^3P_0$, enables us to assess the

gas conditions and content in H1429. Such observations are detailed in Section 2, whose results are used together with the lines reported in M14 to pursue a large velocity gradient (LVG) analysis of the CO + [C I] SLED in Section 3. The implications of the results presented here are discussed in Section 4. Finally, Section 5 presents the concluding remarks.

Throughout this paper, the following Λ cold dark matter (ΛCDM) cosmology is adopted: $H_0 = 70$ km s^{-1} Mpc^{-1}, $\Omega_M = 0.3$, and $\Omega_\Lambda = 0.7$. The cosmic microwave background (CMB) is assumed to expand adiabatically ($T_z = T_0 \times (1+z)$, with $T_0 = 2.726$; Muller et al. 2013). When stated, the gas mass estimates are corrected by a factor of 1.36 to account for chemical elements heavier than hydrogen, assuming the latter comprises 73–74 per cent of the total baryonic matter mass (Croswell 1996; Carroll & Ostlie 2006).

2 OBSERVATIONS

Prior to this work, only CO $J_{up} = [2,4,5]$, [C I] $^3P_1 - ^3P_0$, and CS (10–9) had been observed toward H1429−0028. The limited number of spectral features precluded a reliable analysis of the molecular gas content in the system. It was not clear if a two-component CO SLED existed and, given the redshifts of the lens ($z = 0.218$) and sources ($z = 1.027$), there was the possibility that the background CO (5–4) emission measured by Z-Spec at APEX was contaminated by foreground CO (3–2) emission. This work makes use of the previously detected lines in addition to recent observations of CO $J_{up} = [3,6]$ transitions to remove the ambiguities mentioned. The new observations are described in the following subsections.

2.1 APEX

The instrument suite available at the Atacama Pathfinder EXperiment (APEX) has contributed strongly toward the understanding of H1429−0028, giving the initial redshift determination of the system and detecting four CO transitions. The Z-Spec observations targeting the CO transitions J = 4–3 and 5–4 were already described in detail in M14. Here, we proceed to describe the more recent SEPIA Band 5 and SHeFI APEX2 observations.

2.1.1 SEPIA Band 5

The CO (3–2) and CS (7–6) transitions were targeted with APEX/SEPIA-Band 5 between 2016 May 25 and June 5 (097.A–0995, PI: Messias). The lower side (signal) band was tuned to 170 GHz to cover the two lines of interest, putting the upper side (image) band at 182 GHz. The observations were conducted under precipitable water vapor (PWV) ∼ 3 mm (ranging from 2.6 to 5.1 mm between 2016 May 25 and June 1, and 1.3–1.7 mm on 2016 June 5) using either Jupiter or Mars as calibrators. A standard observing strategy was adopted (wobbler switching with a 50 arcmin amplitude, at a frequency of 0.5 Hz). The total time on source was 5.1 h. The data were reduced with CLASS (a GILDAS[1] task). The rms uncertainty on the final co-added spectrum is 0.3 mK (12 mJy) at a spectral resolution of 100 km s^{-1}. The adopted Kelvin to Jansky conversion factor is 38.4 Jy/K (Belitsky et al. 2018).

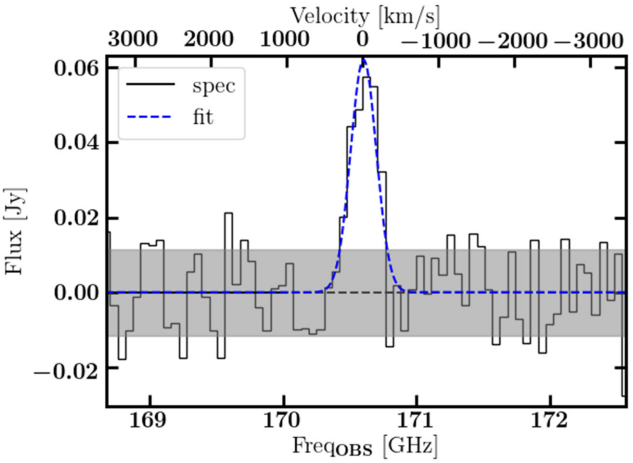

Figure 2. The SEPIA-Band 5 spectrum targeting CO (3–2) transition. The observed spectrum is shown as the solid black histogram. The Gaussian fit to the line emission is shown as a dashed blue line. The velocity frame used in the upper axis is set to $z = 1.027$. The shaded grey region shows the $\pm 1\sigma$ uncertainty.

2.1.2 SHeFI APEX2

The CO (6–5) transition was targeted with APEX/SHeFI-APEX2 on 2016 June 5 and between 2016 July 29 and August 4 (097.A-0995, PI: Messias). The lower side (signal) band was tuned to 339.8 GHz to cover the line of interest and CS (14–13), putting the upper side (image) band at 351.8 GHz. The observations were conducted under PWV = 0.55–1.4 mm, using IRAS 15194−5115, SW Vir, and SgrB2(N) as calibrators. A standard observing strategy was adopted (wobbler switching with a 50 arcmin amplitude, at a frequency of 0.5 Hz). The total time on source was 4 h. The data were reduced with CLASS (a GILDAS task). The rms uncertainty on the final co-added spectrum is 0.6 mK (24 mJy) at a spectral resolution of 100 km s^{-1}. The adopted Kelvin to Jansky conversion factor is 40.8 Jy/K following the procedure reported in the APEX website.[2]

3 RESULTS

3.1 Properties of targeted lines

Altogether, three chemical species (C, CO, and CS) and nine transitions have been targeted thus far (M14 and this work). Of these, only CS (7–6) and CS(14–13), observed by APEX, were not detected, as expected by the depths of these observations. Also, since CO (5–4) has not been spectrally resolved thus far, and because of the possibility of foreground line contamination (Section 1.1), this transition is left out of the analysis. Figs 2 and 3 show the newly targeted CO transitions J = 3–2 and 6–5 as observed by SEPIA-Band 5 and SHeFI-APEX2, respectively.

Fig. 4 compares the line profiles of the CO transitions detected to date. As already mentioned in M14, the J = 2–1 and 4–3 transitions show a double-peak or plateau line profile. These new APEX observations actually follow this scenario, where the blueshifted component is stronger at low-J transitions (and almost absent at J = 6–5), while the redshifted one is stronger at high-J transitions. This could be a consequence of the red component being more

[1] http://www.iram.fr/IRAMFR/GILDAS

[2] http://www.apex-telescope.org/telescope/efficiency/index.php

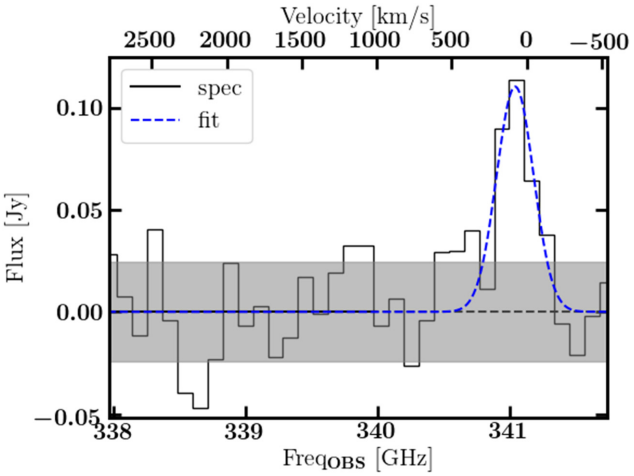

Figure 3. The same as in Fig. 2, but for the SHeFI-APEX2 spectrum targeting CO (6–5) transition.

excited than the blue one as a result of the merger. Henceforth, these blue and red velocity components are referred to as components I and II, respectively.

Interestingly, the additional flux at even higher velocities (∼500 km s^{-1}, also mentioned in M14; component III henceforth) matches the excess flux seen at ∼500 km s^{-1} in the J = 6–5 spectrum. This could be evidence for a shock-induced component, like an outflow. Because of this result, we revisited the *Hubble Space Telescope* (*HST*) grism data assessing any possible emission from the arc-like feature external to the Einstein ring (best seen in *HST*/Wide Field Camera 3 (WFC3)-*F110W* imaging), in search of evidence of a velocity match between that component and the redshifted one reported here. However, due to the depth of the data and to neighbouring source contamination, no emission is observed. The location and morphology of this feature are addressed later in Section 3.3.

3.2 Spectral line decomposition

The spectral decomposition of the line profiles into the three possible spectral components mentioned in the previous section was made in a train-and-fit approach. First, a three-Gaussian fit to the spatially integrated CO (4–3) spectrum was pursued as a training step by making use of the PYTHON implementation of the affine-invariant ensemble sampler for Markov chain Monte Carlo (MCMC) proposed by Goodman & Weare (2010), EMCEE (Foreman-Mackey et al. 2013). This transition was chosen being the one with the highest signal-to-noise ratio allowing for a better line profile characterization, and the result can be seen in Fig. 5. The training-derived values of the three centroid velocities were kept fixed while fitting the remainder of the spectrally resolved CO transition spectra. The training-derived Gaussian full width at half-maximum (FWHM) values of each component were considered as first guesses. Based on the line profile discussion in Section 3.1 (see also Fig. 4), the flux contribution of each velocity component to each spectrum total flux of a given J → J − 1 rotational transition ($\mathcal{C}^i_{\rm J,J-1} = S^i/S^{\rm TOT}$, where S^i is the velocity-integrated flux of a given velocity component $i \equiv$ [I, II, III], and $S^{\rm TOT}$ the total velocity-integrated flux) had to comply with the following priors: $\mathcal{C}^{\rm I}_{21} > \mathcal{C}^{\rm I}_{32} > \mathcal{C}^{\rm I}_{43} > \mathcal{C}^{\rm I}_{65}$, $\mathcal{C}^{\rm II,III}_{21} < \mathcal{C}^{\rm II,III}_{32} < \mathcal{C}^{\rm II,III}_{43} < \mathcal{C}^{\rm II,III}_{65}$. Note that the $\mathcal{C}_{43}$ values are those corresponding to the 50th percentile reported from the training step. While fitting the [C I] $^3P_1$−$^3P_0$ profile, both the component centroid velocities and FWHMs were fixed to the 50th percentiles reported from the training step. This was done since, although the line profile shows a plateau, it also reveals a sharp break at ∼180 km s^{-1} and no extra assumptions on the relative component contribution can be adopted like in the other CO transitions.[3] Because of sky-line contamination, component III is not observable in the [C I] transition.

Fig. 6 shows the results of this fitting approach, while Table 1 reports on the velocity-integrated fluxes of each component at each CO and [C I] transitions. The I, II, and III refer to each component ordered by increasing centroid velocity ($v^{\rm I}_{\rm c} = -130^{+6}_{-6}$ km s^{-1}, $v^{\rm II}_{\rm c} = 131^{+5}_{-5}$ km s^{-1}, and $v^{\rm III}_{\rm c} = 500^{+20}_{-30}$ km s^{-1} as measured in CO J = 4–3). Note that components III and I in CO (2–1) and (6–5), respectively, are allowed to be zero, i.e. not to be present, yet the analysis shows that these components are detected at the 3.2σ and 1.4σ levels ($0.9_{-0.3}$ and 11_{-8} Jy km s^{-1}), respectively.

The spectral–spatial decomposition of the three components was also pursued on a pixel-by-pixel basis (i.e. not in the visibility plane). Again, a three-Gaussian fit to the spatially integrated CO(4–3) spectrum was used as a training step. The training-derived values of the centroid velocity and Gaussian FWHM of each component were used as reference for each spectrum fit in each cube pixel, while the relative amplitudes were computed independently for each cube pixel. Fig. 7 shows the result of this spatial–spectral decomposition via the velocity-integrated flux maps (moment-0) of each studied component. The spatial distributions are distinct between the three, hence coming from different regions and this may result in distinct magnifications.

3.3 Differential magnification

Given the extension and multiplicity of the background system, one may wonder whether differential magnification may occur to some degree. In table 3 of M14, the lensing modelling at the time showed a range in the magnification factor between 5 and 11 depending on the spectral band. Since then, new observations have been obtained at much finer spatial resolution (0.12 arcsec; Dye et al. 2018) tracing the dust emission at rest frame 696 GHz (430 μm). These allowed an improvement of the lens model, which resulted in a revised magnification factor of 24 ± 1, twice that reported in M14 (10.8 ± 0.7). Even though the latter was based on slightly lower frequency data (rest frame 474 GHz or 632 μm), both are tracing cold dust via the Rayleigh–Jeans tail of the spectrum, hence the difference between the two results from the improvement in the lensing model.

We have thus revised the source reconstruction of the CO (4–3) emission. Specifically, each moment-0 map of the spectral components (Fig. 7) was reconstructed separately using the same lens model from Dye et al. (2018), and AutoLens (Nightingale, Dye & Massey 2018) was used as an independent check of the lens parameters. The best-fitting result is seen in Fig. 8, where the source areas (A) by counting the number of pixels in the source plane above 3σ are found to be $A^{\rm I} = 0.062$ arcsec^2 (4.1 kpc^2), $A^{\rm II} = 0.039$ arcsec^2 (2.6 kpc^2), and $A^{\rm III} = 0.011$ arcsec^2 (0.72 kpc^2). This new analysis also implies that the current estimate for the dynamical

[3]We revisited the data set to improve the self-calibration step (only in phase) and retrieved the spectrum from the image itself in a common region to CO (4–3) spectrum extraction, not from the model component map as in M14. This resulted in the differences between the [C I] $^3P_1$−$^3P_0$ spectrum shown here and in M14.

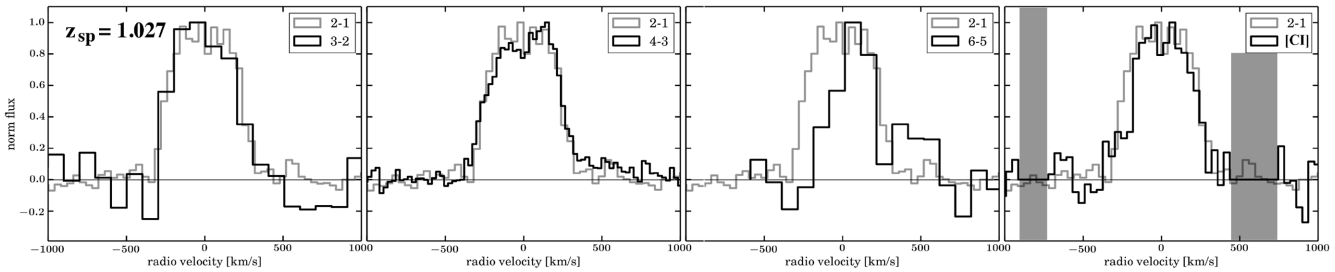

Figure 4. Line profile comparison between the spectrally resolved CO transitions detected to date. In each panel, CO (2–1) is used as reference to ease comparison with CO J = 3–2 (left-hand panel), 4–3 (middle left), 6–5 (middle right), and [C I] $^3P_1-^3P_0$. The line fluxes are normalized to the line peaks. The velocity frame is set to $z_{sp} = 1.027$. The J = 4–3 is displayed at a ∼25 km s^{-1} spectral resolution, J = 2–1 and [C I] at ∼40 km s^{-1}, while J = 3–2 and 6–5 at ∼100 km s^{-1}. This figure shows that there are up to three detected components comprising the line profile in this system: two central main ones blueshifted and redshifted, and another one redshifted to ∼500 km s^{-1}. The latter cannot be assessed in the [C I] transition since it has been flagged due to sky-line contamination (shaded regions).

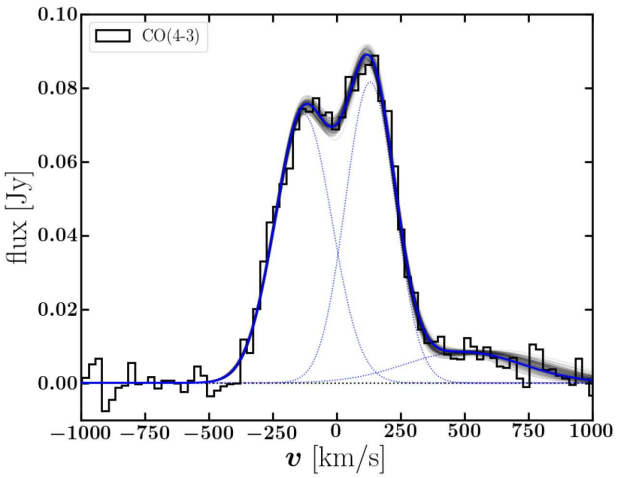

Figure 5. Spectral decomposition of the CO (4–3) transition. The solid black histogram shows the observed spectrum. The solid blue line represents the 50th percentile spectral fit, with each of the three components shown individually as dotted blue lines. The grey thin solid lines are 100 randomly chosen MCMC samples. This analysis served as a training step before fitting the remainder spectrally resolved transitions (Fig. 6). The error level per channel relative to peak is ∼1.2 per cent.

mass and half-light radius of the NS component in the merger is $M_{dyn} = 5^{+3}_{-2} \times 10^{10}$ M$_\odot$ and $r_{1/2} = 0.7^{+0.5}_{-0.3}$ kpc, which are in agreement with the reported values in M14, where the 'isotropic virial estimator' was also assumed: $M_{dyn} = 2.8 \times 10^5 (\Delta v_{FWHM})^2 r_{1/2}$, where $[M_{dyn}] = M_\odot$, Δv_{FWHM} is the CO(4–3) FWHM, and $r_{1/2}$ is the half-light radius in units of kpc.

The magnification profiles for each component are displayed in Fig. 9. These show how the magnification evolves with cumulative source flux (indicated as fraction of total flux), which is estimated by gradually summing source plane pixels in decreasing flux order. It is evident that component III is consistently less magnified than the other two components, which have indistinguishable total magnifications at flux fractions above ∼0.6 within errors. The total magnifications are the following: $\mu^{I} = 15.1 \pm 0.7$, $\mu^{II} = 15.6 \pm 0.4$, and $\mu^{III} = 12 \pm 1$.

Finally, it is worth assessing the differential magnification between each emission line. The other transition resolved into the ring and knot morphology observed in CO(4–3) is [C I] $^3P_1-^3P_0$. The same model from Dye et al. (2018) was applied to the velocity-integrated flux map of [C I]. This time, for the purpose of maximizing signal-to-noise ratio, and since the CO(4–3) analysis pointed to no differential magnification between the velocity components I and II, both of these were analysed together (i.e. no spectral deblending was considered). The spatial distribution of the emission at $>3\sigma$ is displayed in Fig. 8, comprising an area of $A_{[CI]} = 0.046$ arcsec^2 (3.0 kpc^2). The magnification profile is displayed in Fig. 9, where it is seen that it follows those observed in CO(4–3) and its total magnification factor is 16.1 ± 0.6.

As a result, based on the available data, we assume below that the analysis is not affected by differential magnification between velocity components nor between spectral lines. Specifically, we assume that the velocity components I and II are equally magnified and the CO transitions between themselves and with respect to [C I].

3.4 Large velocity gradient analysis

In Section 3.3, we make the case that, within the uncertainties, the differences between the two main spectral components I and II are not affected by differential magnification, but rather from different excitation levels (Daddi et al. 2015; Yang et al. 2017; Cañameras et al. 2018). Also, component III is significantly less magnified and its [C I] emission is unconstrained due to sky-line contamination, preventing a proper analysis of its physical conditions. However, given its brightness, it is expected to account for a relatively minor fraction of the molecular gas budget in the system. Nevertheless, follow-up observations are of interest since this feature will likely help to understand the current stage of evolution of the merger (e.g. if it is confirmed to be an outflow). As a result, this section will focus on the separate analysis of components I and II alone. We note that it does not consider CO (5–4) since it is not spectrally resolved. In the future, high spatial resolution imaging will enable proper multi-J spectral and spatial decomposition of the CO emission as it is shown for CO (4–3) in Section 3.3.

As already mentioned, many transitions were detected thus far towards H1429–0028: CO ($J_{up} = 2, 3, 4, 5, 6$), [C I] ($^3P_1-^3P_0$), and CS (10–9). The former two species are commonly used to indirectly derive the molecular gas content. While CO is brighter, thus easier to detect, the fine structure system of [C I] is characterized by a simple three-level system easily excited by particle collisions, and is believed to be widespread in giant molecular clouds (Tomassetti et al. 2014, and references therein). The CS molecule is regarded as a high-density gas tracer, hence it could be used as well, but this retrieved poor results (e.g. the predicted CO SLED overestimated the high-J transitions' fluxes). This may be a result of CS being

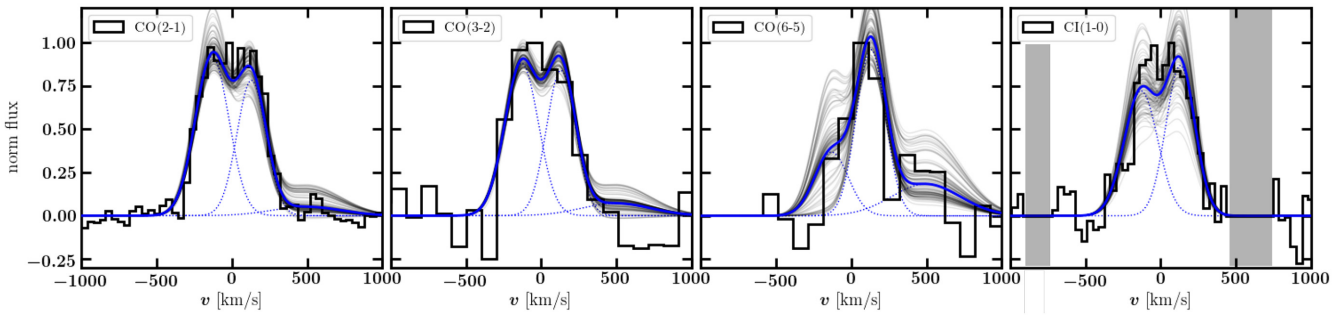

Figure 6. Spectral decomposition of the other spectrally resolved CO and [C I] transitions. The solid black histograms show the observed spectra normalized to maximum flux for comparison purposes. The solid blue line represents the 50th percentile spectral fit, with each of the three components shown individually as dotted blue lines. The grey thin solid lines are 100 randomly chosen MCMC samples. The training step was done by fitting the CO (4–3) transition (Fig. 5). The central velocities of each spectral component were kept fixed. The error level per channel relative to peak is about: 2.6 per cent (left-hand panel), 20 per cent (middle-left panel), 22 per cent (middle-right panel), and 3.2 per cent (right-hand panel). Again, note that the shaded regions in the [C I] panel show the velocity ranges contaminated by atmospheric line.

Table 1. Properties of targeted lines toward H1429−0028 used in the analysis.

Species	Transition	$S\Delta v^{a}_{\rm obs}$ [Jy km s^{-1}]	$S\Delta v^{\rm I}$ [Jy km s^{-1}]	FWHM$^{\rm I}$ [km s^{-1}]	$S\Delta v^{\rm II}$ [Jy km s^{-1}]	FWHM$^{\rm II}$ [km s^{-1}]	$S\Delta v^{\rm III}$ [Jy km s^{-1}]	FWHM$^{\rm III}$ [km s^{-1}]	Facility
CO	2–1	14.4 ± 0.2	$7.7^{+0.7}_{-0.7}$	263^{+5}_{-2}	$5.6^{+0.6}_{-0.8}$	228^{+1}_{-7}	$0.9^{+2}_{-0.3}$	$536.2^{+0.1}_{-4}$	ALMA
	3–2	22 ± 5	$14.3^{+1}_{-0.7}$	$262.7^{+7}_{-0.2}$	$11.7^{+0.9}_{-1}$	$227.6^{+2}_{-0.9}$	2^{+2}_{-1}	536^{+1}_{-2}	APEX
	4–3	44.8 ± 0.4	$20.4^{+0.9}_{-0.9}$	263^{+8}_{-7}	20^{+1}_{-1}	228^{+9}_{-8}	$4.8^{+0.5}_{-0.4}$	540^{+40}_{-40}	ALMA
	6–5	36 ± 10	12^{+5}_{-8}	263^{+4}_{-3}	26^{+4}_{-2}	$227.6^{+0.9}_{-6}$	12^{+11}_{-5}	$536.3^{+5}_{-0.2}$	APEX
[C I]	$^3P_1-^3P_0$	11.9 ± 0.2	$5.7^{+1}_{-0.9}$	$(263)^{b}$	6^{+1}_{-1}	$(228)^{b}$	...	...	ALMA

Note. The central velocities of each component as measured in CO (4–3) are $v_{\rm c}^{\rm I} = -130^{+6}_{-6}$ km s^{-1}, $v_{\rm c}^{\rm II} = 131^{+5}_{-5}$ km s^{-1}, and $v_{\rm c}^{\rm III} = 500^{+20}_{-30}$ km s^{-1}.
[a]Values are those retrieved by integrating the observed spectra from –500 to 1000 km s^{-1} in CO transitions and to 500 km s^{-1} in the [C I] transition.
[b]The FWHM values for each of the two components in [C I] $^3P_1-^3P_0$ were fixed to those measured in CO (4–3).

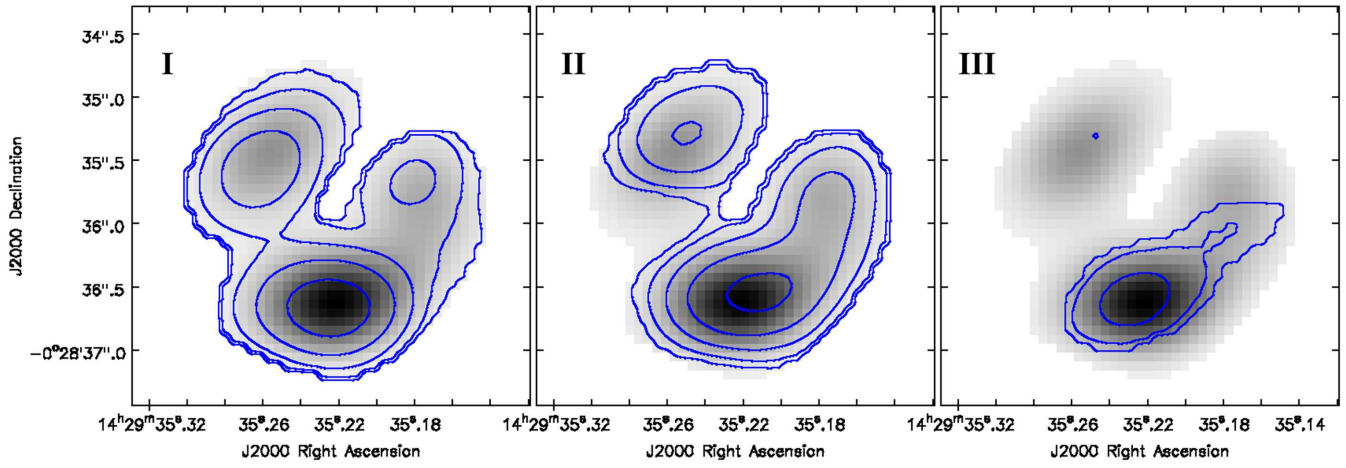

Figure 7. A spectral–spatial decomposition of the three spectral components comprising the CO (4–3) emission. The grey-scale image represents the total velocity-integrated flux map (moment-0). The blue contours in the left-hand, middle, and right-hand panels reveal the emission of, respectively, the components with centroids at around −130 (I), 130 (II), and 500 (III) km s^{-1} away from the systemic velocity. The contour levels are 3σ, 6σ, 12σ, 24σ, and 48σ.

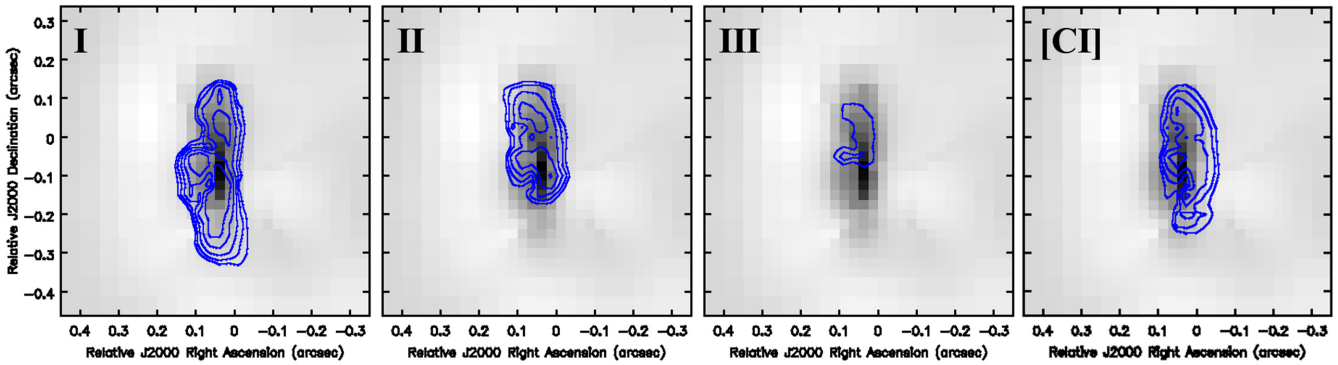

Figure 8. The three panels show the spectral–spatial decomposition in the 0.8×0.8 arcsec^2 source plane of the three spectral components comprising the CO (4–3) emission. The grey-scale image represents the total velocity-integrated flux map (moment-0). The blue contours in the left, middle-left, and middle-right panels reveal the CO (4–3) emission of, respectively, the components with centroids at -130^{+6}_{-6} km s^{-1} (I), $+131^{+5}_{-5}$ km s^{-1} (II), and $+500^{+20}_{-30}$ km s^{-1} (III) away of the systemic velocity. The blue contours in the right-hand panel reveal the [C I] $^3P_1-^3P_0$ velocity-integrate flux map (components I and II were considered together). The contour levels are set at the 3σ, 4.2σ, 6σ, 8.5σ, and 12σ.

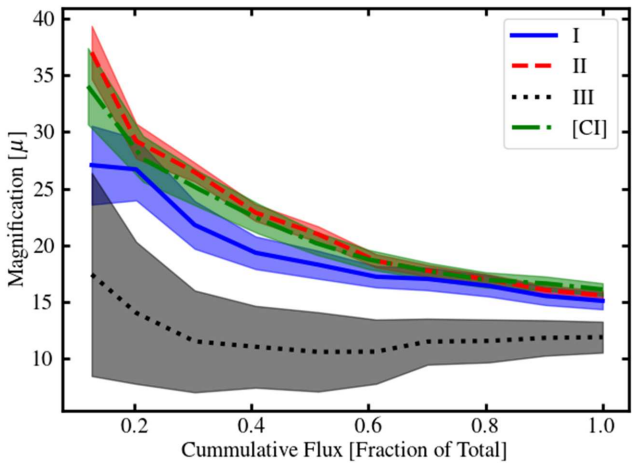

Figure 9. Assessing the differential magnification in H1429−0028. The cumulative source flux (indicated as fraction of total flux) is estimated by gradually summing source plane pixels in decreasing flux order. While components I and II in CO(4–3) are magnified by a comparable amount ($\mu \sim 15$), component III is less magnified ($\mu \sim 12$). The profile of [C I] $^3P_1-^3P_0$ for the combined emission from components I and II is also displayed in green, showing no significant difference with respect to CO(4–3).

detected in a very small region in the system, while CO and C are more extended, which could then result in differential magnification (Fig. 9), further enhancing the difference.

We adopt the large velocity gradient (LVG) formalism to interpret the CO ($J_{up} = 2, 3, 4, 6$) and [C I] SLED by making use of MYRADEX.[4] An escape probability of $\beta = \frac{1-e^{-\tau}}{\tau}$ is assumed in an expanding spherical geometry. The CMB temperature is 5.53 K at $z = 1.027$. The CO line width was set to 262 and 228 km s^{-1} for components I and II, respectively, in accordance to the values in Table 1. The CO and C abundances relative to H_2 (small x_{CO} and x_C) are both assumed to be $\sim 10^{-4}$, which already implies that a significant fraction of carbon is locked into CO (Walter et al. 2011), i.e. the CO emission mostly comes from dense molecular regions (e.g. Wolfire, Hollenbach & McKee 2010; Narayanan et al. 2012). The uncertainty in these abundances is further explored in Section 4.2.

We have adopted different approaches to estimate the gas temperature (T [K]), the molecular number density (n_{H_2} [cm^{-3}]), velocity gradient (dv [m s^{-1} pc^{-1}]), column density (N_{H_2} [cm^{-2}]),[5] and the molecular gas mass (M_{H_2} [M$_\odot$]), while considering CO and [C I] together. The best-fitting value was obtained by finding the minimum χ^2 value in a grid of line intensity values considering conditions ranging $10 < T$ [K] < 1000, $10^2 < n_{H_2}$ [cm^{-3}] $< 10^6$, and $10^2 <$ dv [m s^{-1} pc^{-1}] $< 10^6$, with log steps of 0.1 dex. Maximum likelihood (ML; e.g. Zhang et al. 2014), bootstrapping, and MCMC approaches also adopted this same grid and provided the 16th, 50th, and 84th percentiles. While bootstrapping, a total of 1000 iterations were adopted where, in each one, the observed line flux values were randomly defined to be around the real observed value following a Gaussian distribution with a standard deviation equal to the estimated flux error. This was adopted in all the above approaches, together with a 5 and 10 per cent error in flux added in quadrature to the instrumental error to account for the uncertainty in the absolute flux scaling in CO (2–1) and the remaining transitions, respectively.

This analysis adopted priors in order to better constrain the results. The H_2 mass should not be larger than the dynamical mass ($M_{H_2} < 7.8 \times 10^{10}$ M$_\odot$, $+1\sigma$ of the dynamical mass estimate). It is also assumed that the gas is in virial equilibrium or supervirialized, i.e. the velocity gradient is equal or greater than that calculated from the virial equilibrium ($K_{vir} = (dv/dr)_{LVG}/(dv/dr)_{vir} \geq 1$) as expected from normal to starburst galaxies (e.g. Papadopoulos & Seaquist 1999; Zhang et al. 2014).

Figs 10 and 11 show the results graphically for the analysis of CO and [C I] for components I and II, respectively, while Table 2 presents the results quantitatively. In the figures, the top left-hand panel shows the observed CO SLED and the best fit (solid black line) and range of acceptable models (shaded grey regions). In the remaining plots, the central panel shows the surface likelihood distribution, with the best-fitting value appearing as an open red circle. Also, the MCMC (red) and bootstrapping (blue) results appear as error bars, where their centre indicates the 50th percentile, and the extremes the 16th and 84th percentiles. These

[4] https://github.com/fjdu/myRadex

[5] Note that the following is assumed: $N_{H_2} = n_{H_2} \frac{\text{line}_{FWHM}}{dv} x_{C,CO}$.

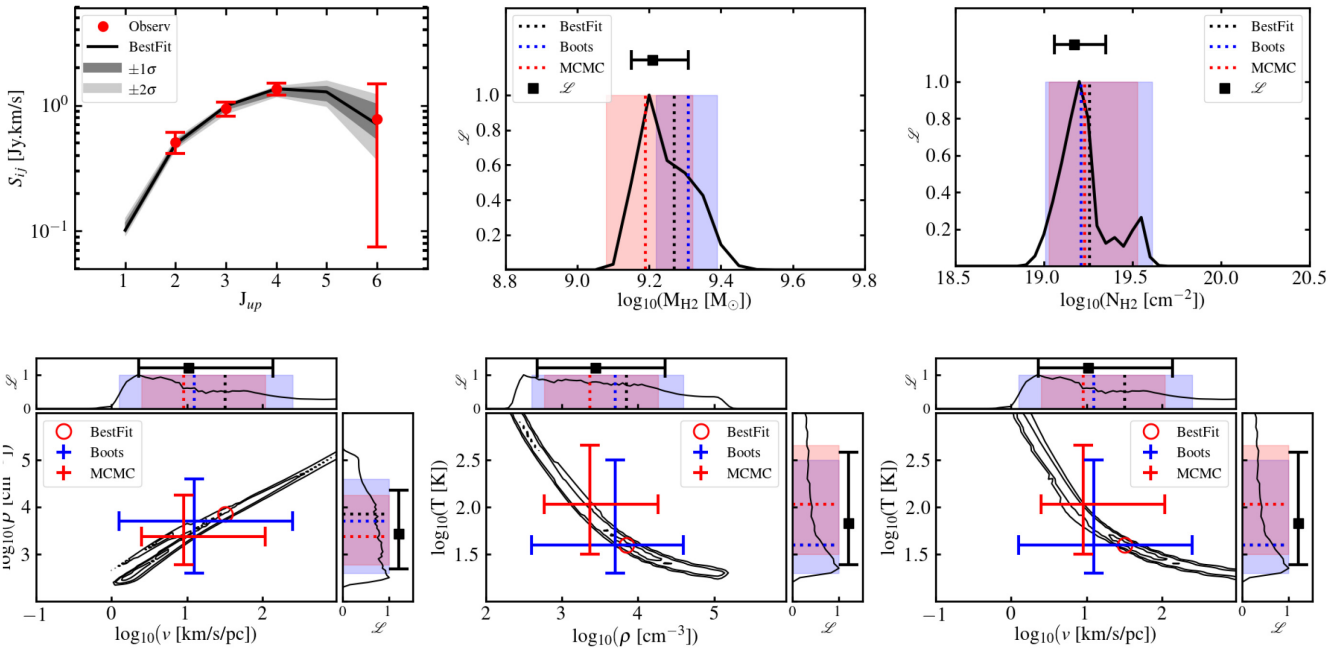

Figure 10. Modelling H1429–0028's CO and [C I] SLED with MYRADEX for component I. Top left: the solid black line shows the best fit to the CO SLED, while the dark and light grey shaded regions show the 16th–84th and 2nd–98th percentile ranges of the model predicted fluxes resulting from the maximum likelihood analysis. Top middle and right: these panels show the likelihood distributions of the H_2 mass and column density and their 15.9th, 50th, and 84.1th percentile values as error bars. The best-fitting value is marked with a dotted line, while the blue and red dotted lines and transparent regions show the 15.9th, 50th, and 84.1th percentile values for, respectively, the bootstrapping and MCMC analysis. Bottom: these three panels show the probability surface density of the molecular gas density (n_{H_2}), velocity gradient (v), and gas temperature (T), when comparing each with the other two. The top and side plots follow the same colour and pattern coding as the middle and right top panels.

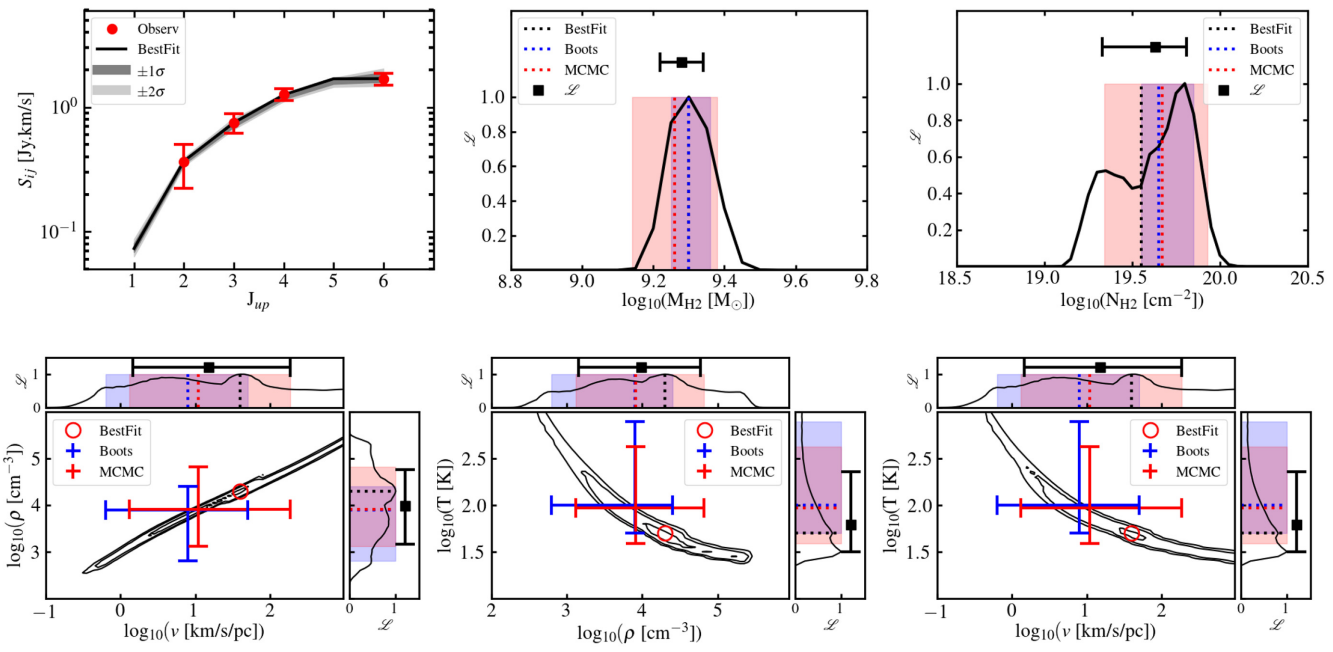

Figure 11. The same as Fig. 10, but for component II.

ranges are again displayed in the top and side panels as transparent regions (vertical dotted line indicating the 50th percentile). Here, the likelihood distribution for each parameter is shown with a solid line, and its 16th, 50th, and 84th percentiles are displayed with a black error bar. In the side panels, the vertical black line indicates the best-fitting value. For completeness, the predicted

Table 2. CO and [C I] SLED analysis in H1429−0028.

Pars.[a]	χ^2	Boots.	MCMC	ML	Mean[b]
			Component I		
$\log T$	1.60	$1.6^{+0.9}_{-0.3}$	$2.0^{+0.6}_{-0.5}$	$1.8^{+0.8}_{-0.4}$	$1.8^{+0.4}_{-0.3}$
$\log n$	3.85	$3.7^{+0.9}_{-1}$	$3.4^{+0.9}_{-0.6}$	$3.4^{+0.9}_{-0.8}$	$3.5^{+0.5}_{-0.5}$
$\log \mathrm{d}v$	1.50	1^{+1}_{-1}	$1.0^{+1}_{-0.6}$	$1.0^{+1}_{-0.7}$	$1.0^{+0.7}_{-0.4}$
$\log N$	19.26	$19.2^{+0.4}_{-0.2}$	$19.2^{+0.3}_{-0.2}$	$19.2^{+0.2}_{-0.1}$	$19.2^{+0.2}_{-0.1}$
$\log f$	−0.94	$-0.9^{+0.3}_{-0.3}$	$-1.0^{+0.2}_{-0.2}$	$-1.0^{+0.2}_{-0.1}$	$-1.0^{+0.1}_{-0.1}$
$\log M$	9.27	$9.3^{+0.1}_{-0.1}$	$9.2^{+0.1}_{-0.1}$	$9.21^{+0.1}_{-0.06}$	$9.24^{+0.06}_{-0.05}$
			Component II		
$\log T$	1.70	$2.0^{+0.9}_{-0.3}$	$2.0^{+0.7}_{-0.4}$	$1.8^{+0.6}_{-0.3}$	$1.9^{+0.4}_{-0.2}$
$\log n$	4.30	$3.9^{+0.5}_{-1}$	$3.9^{+0.9}_{-0.8}$	$4.0^{+0.8}_{-0.8}$	$3.9^{+0.4}_{-0.5}$
$\log \mathrm{d}v$	1.60	$0.9^{+0.8}_{-1}$	$1.0^{+1}_{-0.9}$	1^{+1}_{-1}	$1.0^{+0.6}_{-0.6}$
$\log N$	19.55	$19.7^{+0.2}_{-0.1}$	$19.7^{+0.3}_{-0.3}$	$19.6^{+0.2}_{-0.3}$	$19.7^{+0.1}_{-0.2}$
$\log f$	−1.00	$-1.1^{+0.2}_{-0.2}$	$-1.2^{+0.3}_{-0.2}$	$-1.1^{+0.3}_{-0.2}$	$-1.1^{+0.2}_{-0.1}$
$\log M$	9.30	$9.3^{+0.1}_{-0.1}$	$9.3^{+0.1}_{-0.1}$	$9.28^{+0.06}_{-0.06}$	$9.28^{+0.05}_{-0.05}$

[a]The parameters in this column are: temperature, $\log T \equiv \log(T\,[\mathrm{K}])$; molecular gas density, $\log n \equiv \log(n_{\mathrm{H_2}}\,[\mathrm{cm^{-3}}])$; velocity gradient, $\log \mathrm{d}v \equiv \log(\mathrm{d}v\,[\mathrm{m\ s^{-1}\ pc^{-1}}])$; gas column density, $\log N \equiv \log(N_{\mathrm{H_2}}\,[\mathrm{cm^{-2}}])$; area filling factor, $\log f \equiv \log(\langle L^i_{\mathrm{obs}}/L^i_{\mathrm{LVG}}\rangle_{\mathrm{weighted}})$; and molecular gas mass, $\log M \equiv \log(M_{\mathrm{H_2}}\,[\mathrm{M_\odot}])$.
[b]This column shows the log mean between the ML, MCMC, and bootstrap values.

[C I] $^3P_1-{}^3P_0$ velocity-integrated unmagnified flux for components I and II together is $0.72^{+0.1}_{-0.09}$ Jy km s^{-1}, which comprises the observed value of 0.77 ± 0.09.

4 DISCUSSION

4.1 Gas conditions

From Table 2 and Figs 10 and 11, one can see that temperature, velocity gradient, and gas density are poorly constrained and correlated. As a result, there is no significant difference within the errors in these properties between the two velocity components. The molecular gas column density and mass are better constrained, and, although both velocity components have comparable gas masses ($\log(M_{\mathrm{H_2}}\,[\mathrm{M_\odot}]) \sim 9.26$), the column density is $>1\sigma$ higher in II ($\log(N_{\mathrm{H_2}}\,[\mathrm{cm^{-2}}]) = 19.7_{-0.2}$ versus $19.2^{+0.2}$ in I).

Combined, components I and II have $M_{\mathrm{H_2}} = 3.6^{+0.5}_{-0.6} \times 10^9\,\mathrm{M_\odot}$ (where the errors assume the full range of uncertainty from all methods). For reference, this means that the H_2-to-dynamical mass fraction (i.e. $M_{\mathrm{H_2}}/M_{\mathrm{dyn}}$) in the NS component is 8^{+3}_{-6} per cent.

The CO SLED seems to be intermediate between those observed on average in SMGs and quasi-stellar objects (QSOs, Fig. 12; Carilli & Walter 2013; Oteo et al. 2017b). Nevertheless, compared to the CO transitions luminosity ratios presented by Carilli & Walter (2013, table 2 therein), the resemblance to SMG-like ratios is strong: $L'_{32}/L'_{21} = 0.7 \pm 0.2$, $L'_{43}/L'_{21} = 0.78 \pm 0.09$, and $L'_{54}/L'_{21} = 0.45 \pm 0.08$ versus, respectively, average values of 0.78, 0.54, and 0.46 for SMGs or 0.98, 0.88, and 0.70 for QSOs (Carilli & Walter 2013). Given the uncertainties and the current lack of evidence supporting the presence of an accreting supermassive black hole (Timmons et al. 2015; Ma et al. 2018), H1429–0028 is regarded as a DSFG.

Last, but not least, the gas conditions explaining the CO + [C I] SLED predict a CS (10–9) line flux ∼200 times lower than observed. This indicates that there is either a warm component inducing the population of higher J-levels in the CO ladder, or the CS (10–9) emission is a result of differential magnification or chemical segregation in the background system. Follow-up observations of higher J-levels or deeper Atacama Large Millimeter/submillimeter Array (ALMA) imaging can address this issue and the incidence of the high-velocity ($\sim +500$ km s^{-1}) component.

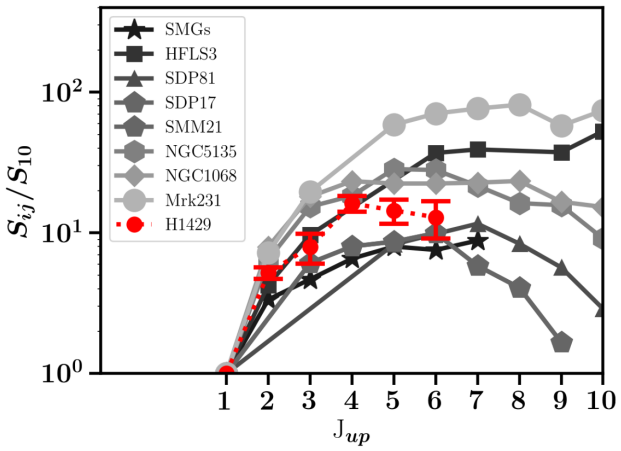

Figure 12. Comparing H1429–0028's CO SLED (the displayed values are total velocity-integrated ones) to other reported in the literature for: local IR luminous galaxies (NGC 5135, NGC 1068, Mrk 231; Rosenberg et al. 2015); SMGs (Bothwell et al. 2013); lensed SMGs (SDP 81, SDP 17, SMM J2135–0102, HFLS3; Danielson et al. 2011; Frayer et al. 2011; Harris et al. 2012; Lupu et al. 2012; Riechers et al. 2013; ALMA Partnership et al. 2015). The CO (1–0) flux from H1429–0028 is that predicted from the analysis in Section 3.4.

4.2 Varying CO and carbon abundances

4.2.1 Changing x_C alone

The neutral carbon abundance adopted in the LVG analysis in Section 3.4 is $x_{\mathrm{C}} = 10^{-4}$. This value is comparable to the abundance of

$(8 \pm 4) \times 10^{-5}$ that was found for a sample of submillimetre galaxies and quasar host galaxies at $z > 2$ (Walter et al. 2011), and even in the centres of some local star-forming galaxies (Israel & Baas 2003; Jiao et al. 2017). However, in the literature, lower values are regularly adopted or reported, down to $x_C \sim 10^{-5}$ (Frerking et al. 1989; Sofia et al. 2004; Tomassetti et al. 2014; Israel, Rosenberg & van der Werf 2015; Jiao et al. 2017).

As a first assessment, one can assume local thermal equilibrium (LTE) conditions and estimate the neutral carbon mass using the [C I] $^3P_1 - ^3P_0$ line alone (see section 4.4 in M14 for details on estimating M_{H_2} based on [C I]). Considering a carbon excitation temperature of $T_{ex} = 29 \pm 6$ (Walter et al. 2011) and an observed [C I] luminosity from components I and II together of $L'_{[CI]10} = (2.4 \pm 0.3) \times 10^9$ K km s^{-1} pc^2, one retrieves $M_{[C\,I]} = (3.0 \pm 0.7) \times 10^6$ M$_\odot$. This implies a molecular gas mass of $M_{H_2} = (5 \pm 1) \times 10^9 (x_C/x_C^{alt})$ M$_\odot$, where $x_C = 10^{-4}$ and we have explicitly included the carbon abundance x_C^{alt} as an optional alternative to our adopted value. Within 1σ, this estimated value agrees with the one obtained from the LVG analysis. One can see that the M_{H_2} estimate will vary linearly with the x_C/x_C^{alt} ratio.

We have also redone the LVG analysis assuming $x_{CO} = 10^{-4}$ and $x_C = 3 \times 10^{-5}$. This induces an increase in the M_{H_2} estimate by a similar factor to which the x_C was reduced by (∼3), just as in the LTE assumption above. In this way, the molecular gas mass in components I and II would increase from $\log(M_{H_2}\,[M_\odot]) = 9.24$ to 9.75 and from 9.28 to 9.77, respectively. However, although the best fit provides acceptable physical values, the peaks of the likelihood distributions and the MCMC posteriors imply very low volume densities 10^{2-3} cm^{-3} (even unconstrained in component I within the model grid), and very low velocity gradients unconstrained down to the lowest values in the model grid (d$v = 0.1$ [km s^{-1} pc^{-1}]).

4.2.2 *Assessing a metallicity dependence*

Finally, one can assume that both x_C and x_O are proportional to metallicity (e.g. as in Wolfire et al. 2010 or Narayanan et al. 2012), one arrives to the conclusion that $x_{CO} \propto (Z')^n$, where $Z' = Z/Z_\odot$. The exponent n here is assumed to be dependent on x_C, x_O, and the densities of these atoms, which already points to $n \sim 2$ if one assumes that both C and O originate from the same process (stellar activity), and no CO dissociation occurs due to less shielding effects at lower metallicity.

As a result, we have ran the LVG analysis assuming $x_C = x_C^0 \times 10^{(Z-Z_\odot)}$ and $x_{CO} = x_{CO}^0 \times 10^{2(Z-Z_\odot)}$. Here, x_C^0 and x_{CO}^0 are the neutral carbon and CO abundances, respectively, adopted in Section 3.4, Z is the measured metallicity $12 + \log(O/H) = 8.49$ in H1429−0028 (see Section 4.3.1) and $Z_\odot$ is the solar metallicity (8.69; Asplund et al. 2009). This implies $x_C = 6.3 \times 10^{-5}$ and $x_{CO} = 4.0 \times 10^{-5}$. This approach results in total molecular mass of $M_{H_2} = 5.6^{+0.7}_{-0.9} \times 10^9$ M$_\odot$, which is a factor of 1.6 ± 0.3 higher than the estimate reported in Section 3.4. Again, this factor is comparable to the one x_C was reduced by.

4.2.3 *Accounting for the abundance uncertainty*

As made clear in the previous subsections, the M_{H_2} estimate varies proportionally with the x_C assumption. Hence, as a conservative approach, and specifically considering the spread of the order of ∼40 per cent in the abundances found in the sample studied by Walter et al. (2011), a more realistic error estimate for the molecular gas estimate would be $M_{H_2} = 4^{+3}_{-2} \times 10^9$ M$_\odot$, where the upper error estimate also accounts for the metallicity-dependent uncertainty discussed in Section 4.2.2. This implies an H_2-to-dynamical mass fraction in the NS component of 8^{+6}_{-7} per cent.

4.3 CO-to-H_2 conversion factor

The CO/[C I] SLED analysis pursued in Section 3.4 (Figs 10 and 11) implies a velocity-integrated J = 1–0 line flux of 180^{+20}_{-20} mJy km s^{-1}, implying a line luminosity of $L'_{CO10} = 1.0^{+0.1}_{-0.1} \times 10^{10}$ K km s^{-1} pc^2 (assuming a magnification of $\mu_{CO} \sim 15$, Section 3.3). This implies that the CO-to-H_2 conversion factor in H1429−0028 is $\alpha_{CO} = M_{H_2}/L'_{CO10} = 0.4^{+0.3}_{-0.2}$ M$_\odot$/(K km s^{-1} pc^2), assuming $M_{H_2} = 4^{+3}_{-2} \times 10^9$ M$_\odot$.

4.3.1 *Comparison with metallicity-dependent α_{CO} relations*

As it has been proposed in the literature (see Bolatto, Wolfire & Leroy 2013, for a review), the CO-to-H_2 conversion factor ($M_{H_2+He} = \alpha_{CO} L'_{CO10}$, $[\alpha_{CO}] = M_\odot/(K\,km\,s^{-1}\,pc^2)$) appears to be dependent on gas phase metallicity, where CO gradually becomes a poor tracer of H_2 with decreasing metallicity.

Using 0.8–1.7 μm grism data acquired by *HST*/WFC3, Timmons et al. (2015) assessed the gas phase metallicity, 12 + log(O/H), for H1429−0028. Their analysis revealed the A+B knot (fig. 1 in M14) as the brightest line emitter in the Einstein ring, resembling the knot flux ratios seen at long wavelengths ($\lambda \gtrsim 1$ mm), and in contrast with the rest-frame optical ones. This points to the fact that line emission is dominated by the NS oriented component in the background system (fig. 8 in M14) also dominating the long-wavelength spectral range.

Following the linear relation proposed by Sobral et al. (2015) between Hα/[N II] flux ratios and the logarithm of the Hα + [N II] equivalent width, one can use the former to estimate the metallicity based on the N2-index relations proposed by Denicoló, Terlevich & Terlevich (2002) and Pettini & Pagel (2004), giving, respectively, $12 + \log(O/H) = 8.7 \pm 0.2$ and 8.6 ± 0.2. Since the N2-index is known to saturate at metallicities close to solar, Pettini & Pagel (2004) proposed the O3N2-index that yields 8.5 ± 0.2. Assuming a solar metallicity of 8.69 (Asplund et al. 2009), H1429−0028 is observed as a system with a metallicity close to solar (e.g. O3N2 estimate is 1.3σ away).

Following the metallicity–[α_{CO}] relation proposed by Genzel et al. (2012, which is based on the N2 calibration by Denicoló et al. 2002), α_{CO} is found to be 5.3 M$_\odot$/(K km s^{-1} pc^2) (with an error factor of ∼1.7).[6] Based on the theoretical predictions by Wolfire et al. (2010) and Glover & Mac Low (2011) (which Bolatto et al. 2013, show to best explain observations), and the empirical metallicity values just mentioned, the expected α_{CO} is very much Milky Way-like (∼4.3–7 M$_\odot$/(K km s^{-1} pc^2)). An alternative theoretical approach by Narayanan et al. (2012) predicts a relation between α_{CO} and both metallicity and CO line intensity. This yields $\alpha_{CO} = 6 \pm 2$ M$_\odot$/(K km s^{-1} pc^2), assuming the O3N2 metallicity index value and the $<W_{CO}>$ as measured in the source plane CO(4–3) moment-0 map scaled to the CO(1–0) flux predicted from the SLED analysis.

However, as briefly noted in M14, such high α_{CO} values imply M_{H_2} values (∼6–8 × 10^{10} M$_\odot$) comparable or higher than the

[6]The reported error factor considers instrumental error alone, and not the scatter of the relation proposed by Genzel et al. (2012).

estimated dynamical mass ($M_{\rm dyn} = 5^{+3}_{-2} \times 10^{10}$ M$_\odot$). As a result, these are deemed not realistic in the case of H1429−0028.

4.3.2 *Comparison with the $L_{\nu_{850\,\mu m}}$–$L'_{\rm CO}$ relation*

Since spectral line observations are time-consuming, the statistical approach proposed by Scoville et al. (2016, see also Hughes et al. 2017; Liang et al. 2018), where the dust continuum is used as a tracer of molecular gas, has become increasingly popular, since one can study numerous galaxies in a very inexpensive way. For completeness, the application of this relation to the case of H1429−0028 is reported here. We note however that the relation assumes a constant galactic-like $\alpha_{\rm CO} = 6.5$ M$_\odot$/(K km s^{-1} pc^2) ,[7] hence what should actually be compared here is CO(1–0) luminosity. Following equation (16) in Scoville et al. (2016, appendix A.6), we assume a power-law index of 3.9 ± 0.4 (M14) instead of 3.8, and $\alpha_{850} = (7 \pm 2) \times 10^{19}$ erg/(s Hz M$_\odot$). We also consider the MBB_EMCEE[8] SED fit to 0.1–1.28 mm photometry in M14 to predict the observed flux at rest frame 850 μm, which avoids the need for the Rayleigh–Jeans approximation correction. This implies $M_{\rm H_2} = 2^{+1}_{-1} \times 10^9$ M$_\odot$ and $L'_{\rm CO10} = 4^{+2}_{-2} \times 10^8$ K km s^{-1} pc^2. While the $M_{\rm H_2}$ mass estimate comprises the SLED analysis result, the CO(1–0) luminosity is a factor of 30^{+10}_{-20} lower than the predicted one (see values summarized in Section 4.3). Nevertheless, H1429−0028 is a lensed galaxy and the errors are still relatively large. As a result, for the time being, this predicted luminosity 1.8σ difference ought to be considered as statistically insignificant.

4.4 The different ISM contents in the two background components

To the depth of the current observations, it is observed that the gas and dust emissions are totally dominated by the NS component. Since the 1.28 mm observations are probing the Rayleigh–Jeans tail of the dust continuum, we can use that information as a tracer of the ISM gas in the system (Scoville et al. 2016). Here, we chose to use this property to assess the relative ISM content between the EW and NS components. From table 2 in M14, it is observed that the total 1.28 mm flux is 6 ± 1 mJy (all assigned to the NS component), while the observations reached an rms of 78 μJy, meaning a 3σ upper limit of 0.23 mJy. Based on the latest lensing model, the magnification factors for the NS and EW components are 24 ± 1 and 11 ± 1, respectively.[9] As a result, the EW gas and dust content is $<9^{+9}$ per cent [10] of that observed in the NS component (i.e. $M_{\rm H_2}$ [M$_\odot$] $< 3^{+4} \times 10^8$). A more direct comparison requires deeper 1 mm dust continuum data or higher spatial resolution observations of low-J transitions ($J_{\rm up} \leq 3$), where a less excited CO SLED from the EW component is expected to peak, and NIR spectral observations to assess the dynamic properties of the EW component.

[7]Note this value already includes a factor of 1.36 to account for elements heavier than hydrogen.
[8]https://github.com/aconley/mbb_emcee
[9]The adopted magnification factor for this component is that measured at $K_{\rm s}$ band, emission that is dominated by the EW component.
[10]The uncertainty here takes into account a factor of 2 in uncertainty to account for dust-to-gas ratio variations.

4.5 Comparison with SED fitting analysis

In M14, we adopted a two-step approach to retrieve the background emission uncontaminated by the foreground one. We used GALFIT in the high spatial resolution *F110W*, *H*, and $K_{\rm s}$ bands imaging to deblend foreground and background emission. Based on this, we later used MAGPHYS (adopting the default low-z template library; da Cunha, Charlot & Elbaz 2008) to determine the foreground emission in the remainder low spatial resolution imaging. On top of this, we further corrected the background rest-frame UV/optical emission for foreground obscuration (adopting different scenarios and taking them into account in the photometry error budget) and differential magnification. Nevertheless, Ma et al. (2018) has recently shown that, even after this considered approach, depending on the star formation history assumed for the template library used for the SED fitting, one can retrieve significantly different conclusions. Also, Zhang et al. (2018) also show that the initial mass function in sources alike H1429 may be top heavy, which was not considered in M14 nor Ma et al. (2018). Although these issues affect even unlensed systems, H1429 has also been shown to be comprised by two spatially separated components, one dominating the UV/optical spectral range, the other the FIR-radio one. This goes against the underlying assumption of both MAGPHYS and CIGALE (Noll et al. 2009) where the stellar and dust components are cospatial.

As a result, in this paper, we avoid any discussion involving conclusions based on the SED fitting done in previous works. Since the molecular and dust content is mostly dominated by the NS component, this work is essentially a description of its properties based on the mm observations reported here and in M14.

5 CONCLUSIONS

In this paper, the gravitationally lensed galaxy merger HATLAS J142935.3–002836 (H1429–0028) at $z = 1.027$ presented in Messias et al. (2014) is characterized in further detail. Specifically, recent APEX observations with SHeFI-APEX2 and the recent SEPIA-Band 5 instrument targeting, respectively, the CO transitions J = 6–5 and 3–2, allowed us to assess the ISM gas content in the background system.

Thanks to the recent APEX observations and previous ALMA ones, a continuous coverage of the CO-SLED from $J_{\rm up} = 2$–6 is now available, together with the [C I] $^3P_1$–$^3P_0$ transition. We have identified three different velocity components comprising the spectra with velocity centroids at $v_{\rm c}^{\rm I} = -130^{+6}_{-6}$ km s^{-1}, $v_{\rm c}^{\rm II} = 131^{+5}_{-5}$ km s^{-1}, and $v_{\rm c}^{\rm III} = 500^{+20}_{-30}$ km s^{-1} (Section 3.2). It is observed that they contribute differently to each transition, but, based on the updated lensing model, we find that the two brightest components are equally magnified by a factor of ∼15, while the fainter one is magnified by ∼12. We also show that the high-velocity component is morphologically much smaller than the others, which seems to agree with its expected higher degree of excitation. Only the two main components I and II were considered in the analysis, since the high velocity one is unconstrained in the [C I] spectrum; see Sections 3.1, 3.2, and 3.3.

Assuming a large velocity gradient scenario and a combined statistical approach (ML, MCMC, and bootstrap), the molecular gas content in H1429−0028 is estimated to be $M_{\rm H_2} = 4^{+3}_{-2} \times 10^9$ M$_\odot$, where the error accounts for the uncertainty in neutral carbon and CO abundances. This amount of gas comprises about 8^{+6}_{-7} per cent of the dynamical mass in the NS component. As a result, at the time of observation, this star formation event is expected to turn only up to 15 per cent (1σ upper limit) of the total (dynamical) mass

into stars. No major excitation differences between components I and II are observed, but the column density is apparently higher toward component I. Averaging over the many statistical approaches and over the two main velocity components, the gas temperature, volume density, and velocity gradient are constrained within a factor of 3 on a galaxy-wide view. These parameters are estimated to be $T \sim 70$ K, $\log(n[\mathrm{cm}^{-3}]) \sim 3.7$, and $\mathrm{d}v \sim 10$ km s^{-1} pc^{-1}. The gas column density is constrained within a factor of 1.4 to be $\log(N[\mathrm{cm}^{-2}]) \sim 19.4$; see Sections 3.4 and 4.2.

Compared to galaxy samples in the literature, H1429−0028 is observed to have a DSFG-like CO-SLED [in line with the lack of evidence thus far supporting the presence of active galactic nucleus (AGN); Timmons et al. 2015; Ma et al. 2018] and, based on the predicted CO (1–0) velocity-integrated flux, a CO-to-H_2 conversion factor ($\alpha_{\mathrm{CO}} = 0.4^{+0.3}_{-0.2}$ M$_\odot$/(K km s^{-1} pc^2)); see Section 4.1.

The spatially resolved dust continuum map allows us to have a first assessment of the relative ISM gas content between the two background components. We estimate that the EW component is very gas and dust poor with a content less than 9^{+9} per cent of what is observed toward the NS component (i.e. $M^{\mathrm{EW}}_{\mathrm{H_2}} < 3^{+4} \times 10^8$ M$_\odot$); see Section 4.4.

ACKNOWLEDGEMENTS

The team thanks the anonymous referee for the careful reading and for the suggestions which helped clarifying the idea needed to be conveyed and the implications of the uncertainties in the analysis.

HM thanks the opportunity given by the ALMA Partnership to work at the Joint ALMA Observatory via its fellowship programme. HM acknowledges support by FCT via the post-doctoral fellowship SFRH/BPD/97986/2013.

We thank insightful discussion with Paola Di Matteo from the GalMer team while attempting to understand this system by the use of galaxy-merger models.

We thank the comments provided by Asantha Cooray.

NN acknowledges support from Conicyt (PIA ACT172033, Fondecyt 1171506, and BASAL AFB-170002).

Z-YZ and IO acknowledge support from the European Research Council in the form of the Advanced Investigator Programme, 321302, COSMICISM.

SD is supported by the UK STFC Rutherford Fellowship scheme.

EI acknowledges partial support from FONDECYT through grant N° 1171710.

DR acknowledges support from the National Science Foundation under grant number AST-1614213.

MJM acknowledges the support of the National Science Centre, Poland through the POLONEZ grant 2015/19/P/ST9/04010; this project has received funding from the European Union's Horizon 2020 research and innovation programme under the Marie Skłodowska-Curie grant agreement no. 665778.

This work is based on data products from observations made with APEX telescope under programmes IDs C-087.F- 0015B-2011, 087.A-0820, 088.A- 1004, and 097.A-0995.

This paper makes use of the following ALMA data: ADS/JAO.ALMA#2011.0.00476.S. ALMA is a partnership of ESO (representing its member states), NSF (USA), and NINS (Japan), together with NRC (Canada), MOST and ASIAA (Taiwan), and KASI (Republic of Korea), in cooperation with the Republic of Chile. The Joint ALMA Observatory is operated by ESO, AUI/NRAO, and NAOJ.

This research made use of IPYTHON (Pérez & Granger 2007), NUMPY (Van Der Walt, Colbert & Varoquaux 2011), MATPLOTLIB (Hunter 2007), SCIPY (Jones et al. 2001), and ASTROPY (a community developed core PYTHON package for Astronomy, ASTROPY Collaboration et al. 2013).

REFERENCES

ALMA Partnership et al., 2015, ApJ, 808, L4
Asplund M., Grevesse N., Sauval A. J., Scott P., 2009, ARA&A, 47, 481
Astropy Collaboration et al., 2013, A&A, 558, A33
Belitsky V. et al., 2018, A&A, 612, A23
Bolatto A. D., Wolfire M., Leroy A. K., 2013, ARA&A, 51, 207
Bothwell M. S. et al., 2013, MNRAS, 429, 3047
Bothwell M. S. et al., 2017, MNRAS, 466, 2825
Calanog J. A. et al., 2014, ApJ, 797, 138
Cañameras R., Yang C., Nesvadba N. P. H. et al., 2018, A&A, 602, 26
Carilli C. L., Walter F., 2013, ARA&A, 51, 105
Carroll B. W., Ostlie D. A., 2006, An Introduction to Modern Astrophysics and Cosmology, 2nd edn. Pearson, Addison-Wesley, San Francisco
Casey C. M., Narayanan D., Cooray A., 2014, Phys. Rep., 541, 45
Croswell K., 1996, The Alchemy of the Heavens. Oxford Univ. Press, Oxford
da Cunha E., Charlot S., Elbaz D., 2008, MNRAS, 388, 1595
Daddi E. et al., 2015, A&A, 577, A46
Danielson A. L. R. et al., 2011, MNRAS, 410, 1687
Denicoló G., Terlevich R., Terlevich E., 2002, MNRAS, 330, 69
Dye S. et al., 2018, MNRAS, 476, 4383
Eales S. et al., 2010, PASP, 122, 499
Foreman-Mackey D., Hogg D. W., Lang D., Goodman J., 2013, PASP, 125, 306
Frayer D. T. et al., 2011, ApJ, 726, L22
Frerking M. A., Keene J., Blake G. A., Phillips T. G., 1989, ApJ, 344, 311
Genzel R. et al., 2012, ApJ, 746, 69
Glover S. C. O., Mac Low M.-M., 2011, MNRAS, 412, 337
Goodman J., Weare J., 2010, Commun. Appl. Math. Comput. Sci., 5, 65
Harris A. I. et al., 2012, ApJ, 752, 152
Hughes D. H. et al., 1998, Nature, 394, 241
Hughes T. M. et al., 2017, MNRAS, 468, L103
Hunter J. D., 2007, Comput. Sci. Eng., 9, 90
Israel F. P., Baas F., 2003, A&A, 404, 495
Israel F. P., Rosenberg M. J. F., van der Werf P., 2015, A&A, 578, A95
Jiao Q., Zhao Y., Zhu M., Lu N., Gao Y., Zhang Z.-Y., 2017, ApJ, 840, L18
Jones E. et al., 2001, SciPy: Open Source Scientific Tools for Python. Available at: http://www.scipy.org/
Liang L., Feldmann R., Faucher-Giguère C.-A., Kereš D., Hopkins P. F., Hayward C. C., Quataert E., Scoville N. Z., 2018, MNRAS, 478, L83
Lupu R. E. et al., 2012, ApJ, 757, 135
Ma J. et al., 2018, ApJ, 864, 60
Messias H. et al., 2014, A&A, 568, A92 (M14)
Motta V. et al., 2018, ApJ, 863, L16
Muller S. et al., 2013, A&A, 551, A109
Narayanan D., Krumholz M. R., Ostriker E. C., Hernquist L., 2012, MNRAS, 421, 3127
Negrello M. et al., 2010, Science, 330, 800
Negrello M. et al., 2017, MNRAS, 465, 3558
Nightingale J. W., Dye S., Massey R. J., 2018, MNRAS, 478, 4738
Noll S., Burgarella D., Giovannoli E., Buat V., Marcillac D., Muñoz-Mateos J. C., 2009, A&A, 507, 1793
Oliver S. J. et al., 2012, MNRAS, 424, 1614
Oteo I. et al., 2017a, ApJ, 850, 170
Oteo I. et al., 2017b, preprint (arXiv:1707.05329)
Papadopoulos P. P., Seaquist E. R., 1999, ApJ, 516, 114
Pérez F., Granger B. E., 2007, Comput. Sci. Eng., 9, 21
Pettini M., Pagel B. E. J., 2004, MNRAS, 348, L59
Planck Collaboration I, 2016, A&A, 594, A1
Riechers D. A. et al., 2011, ApJ, 733, L12
Riechers D. A. et al., 2013, Nature, 496, 329
Rosenberg M. J. F. et al., 2015, ApJ, 801, 72
Scott K. S. et al., 2011, ApJ, 733, 29

Scoville N. et al., 2016, ApJ, 820, 83
Simpson J. M. et al., 2014, ApJ, 788, 125
Smail I., Ivison R. J., Blain A. W., 1997, ApJ, 490, L5
Sobral D. et al., 2015, MNRAS, 451, 2303
Sofia U. J., Lauroesch J. T., Meyer D. M., Cartledge S. I. B., 2004, ApJ, 605, 272
Strandet M. L. et al., 2016, ApJ, 822, 80
Strandet M. L. et al., 2017, ApJ, 842, L15
Timmons N. et al., 2015, ApJ, 805, 140
Timmons N. et al., 2016, ApJ, 829, 21
Toft S. et al., 2014, ApJ, 782, 68
Tomassetti M., Porciani C., Romano-Díaz E., Ludlow A. D., Papadopoulos P. P., 2014, MNRAS, 445, L124
Trujillo I., Ferré-Mateu A., Balcells M., Vazdekis A., Sánchez-Blázquez P., 2014, ApJ, 780, L20
Van Der Walt S., Colbert S. C., Varoquaux G., 2011, Comput. Sci. Eng., 13, 22
Vieira J. D. et al., 2010, ApJ, 719, 763
Vieira J. D. et al., 2013, Nature, 495, 344
Viero M. P. et al., 2014, ApJS, 210, 22
Walter F., Weiß A., Downes D., Decarli R., Henkel C., 2011, ApJ, 730, 18
Wardlow J. L. et al., 2013, ApJ, 762, 59
Williamson R. et al., 2011, ApJ, 738, 139
Wolfire M. G., Hollenbach D., McKee C. F., 2010, ApJ, 716, 1191
Yang C. et al., 2017, A&A, 608, A144
Zhang Z.-Y. et al., 2014, A&A, 568, A122
Zhang Z.-Y., Romano D., Ivison R. J., Papadopoulos P. P., Matteucci F., 2018, Nature, 558, 260

This paper has been typeset from a TEX/LATEX file prepared by the author.